Article:
Hage, FS, Ramasse, QM orcid.org/0000-0001-7466-2283 and Allen, LJ (2020) Contrast reversal in atomic-scale phonon spectroscopic imaging. Physical Review B, 102 (21). 214111. ISSN 2469-9950

https://doi.org/10.1103/physrevb.102.214111

Contrast reversal in atomic-scale phonon spectroscopic imaging

F. S. Hage [1,2,*] Q. M. Ramasse [1,3,†] and L. J. Allen [4,‡]

[1] *SuperSTEM Laboratory, SciTech Daresbury Campus, Daresbury WA4 4AD, United Kingdom*

[2] *Department of Materials, University of Oxford, Oxford OX1 3PH, United Kingdom*

[3] *School of Physics and Astronomy and School of Chemical and Process Engineering, University of Leeds, Leeds LS2 9JT, United Kingdom*

[4] *School of Physics, University of Melbourne, Parkville, Victoria 3010, Australia*

(Received 24 August 2020; revised 14 October 2020; accepted 3 December 2020; published 18 December 2020)

It was recently shown that phonon spectral mapping of atomic structure is possible in scanning transmission electron microscopy. These results were obtained by deflecting the transmitted beam to detect probe electrons that had been scattered through large momentum transfer into a detector centered at an angle more than twice the radius of the bright-field disk. Atomic-scale spectral maps are still obtained for electrons scattered to angles smaller than the probe convergence angle, albeit at lower contrast and despite the smaller momentum transfers associated with these electrons. It is reported here that apparent reversals of contrast can be observed for these smaller momentum transfers, which is not the case when imaging using probe electrons scattered through larger momentum transfers. This phenomenon can be explained in terms of the channeling of the incident probe. We discuss how such contrast reversals may be avoided and atomic resolution maps reliably obtained.

DOI: 10.1103/PhysRevB.102.214111

I. INTRODUCTION

Improved monochromation of the source in scanning transmission electron microscopy (STEM) means that a resolution better than 10 meV is now achievable in energy-loss spectroscopy [1–5]. This technical development paved the way to an experimental demonstration, supported by simulations, that changes in vibrational modes arising from defects such as interfaces, grain boundaries, and even individual atomic impurities could, in principle, be detected with atomic resolution in STEM [6]. These results offer a new tool for the study of the properties of materials at the atomic scale, complementary to surface science techniques such as inelastic tunneling microscopy, which is also able to probe phonon excitations with atomic sensitivity [7,8]. Using STEM, it was even recently shown that a single substitutional silicon impurity atom in freestanding graphene induces a characteristic, atomically localized modification of the vibrational response [9].

The definitive results showing atomic resolution features in Ref. [6] were obtained by deflecting the transmitted beam to detect probe electrons which had been scattered through large momentum transfer into an electron energy-loss spectroscopy (EELS) detector centered at an angle approximately two times the radius of the bright-field (BF) disk, in other words to angular ranges approaching those used for typical high-angle annular dark-field (HAADF) imaging, also known as Z-contrast imaging. Arguably, atomic-scale variations were also observed when the detector was on the optical axis within the bright-field disk diameter [6] and thus measuring phonon excitation events with smaller momentum transfers. However, this led to significantly reduced contrast.

The possibility of a contrast reversal, which in the context of this paper means that maximum intensity is not on the atomic columns but in the holes between columns, was already hinted at for an on-axis detector in Ref. [6]. Here, we investigate this phenomenon in detail, and we demonstrate a clear reversal of contrast when the detector is on the optical axis, whereas this does not occur when imaging using probe electrons scattered through larger momentum transfers. This phenomenon is confirmed by simulations using the quantum excitation of phonons (QEP) model [10] and can be explained in terms of channeling of the incident probe. We discuss how such contrast reversals may be avoided and atomic resolution maps reliably obtained.

II. EXPERIMENT

Energy-loss spectra were acquired at an acceleration voltage of 60 kV and a probe convergence semiangle of 31.5 mrad, resulting in a probe approximately 1 Å in diameter, using a Nion UltraSTEM 100MC scanning transmission electron microscope equipped with a Gatan Enfinium ERS EEL spectrometer. The spectrometer entrance aperture was on the optical axis and spanned a semiangle of 13 mrad, as shown schematically on a simulated convergent beam electron diffraction (CBED) pattern in Fig. 1(a), where the bright-field disk, whose radius is defined by the semiangle of the probe, is also indicated. The probe was scanned across a hexagonal boron nitride flake (h-BN) with AA′ stacking and oriented in a [0001] zone axis. In this orientation atomic columns consisting of alternating B and N atoms are arranged in a honeycomb pattern [11,12], as shown on the inset of $2 \times 2 \times 2$ unit cells of h-BN in Fig. 1(a), which has been tilted slightly away from the

*fshage@superstem.org

†qmramasse@superstem.org

‡lja@unimelb.edu.au

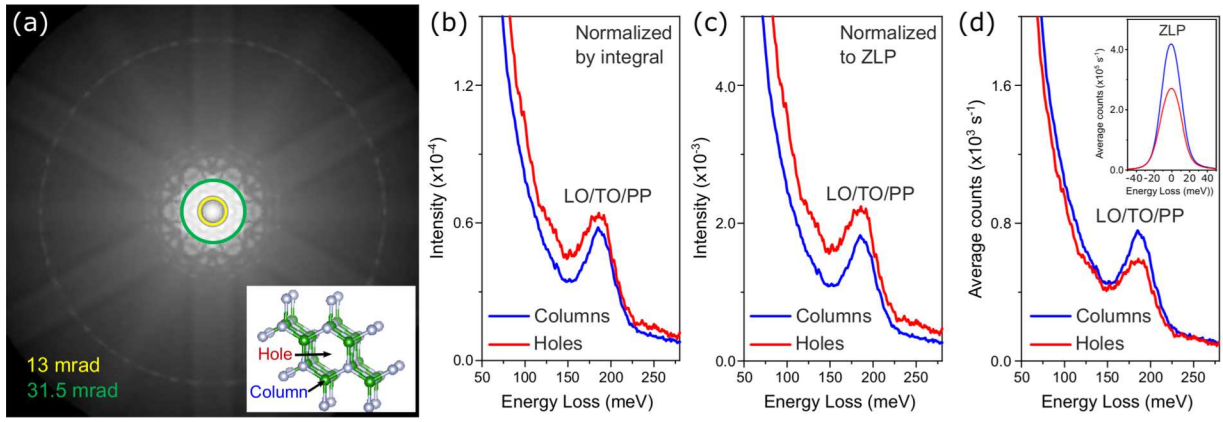

FIG. 1. (a) Schematic showing the detector entrance aperture with a semiangle of 13 mrad (inner yellow circle), as used in the experiment, relative to a simulated convergent-beam electron diffraction pattern for hexagonal BN in the [0001] orientation and of 120 Å thickness (18 unit cells). The larger circle (outer green circle) indicates the extent of the bright-field disk (31.5-mrad semiangle, corresponding to the probe-forming aperture). The BN structure is shown in the inset, indicating probe positions on a column and in the hole at the center of a hexagon. (b) Averaged energy-loss spectra summed over the detector when the probe is on a column of atoms and in the hole between columns, normalized by the integrated spectral intensity between −0.2 and 5 eV energy loss. (c) As in (b), but normalized to the zero-loss peak (ZLP). (d) Unnormalized, averaged energy-loss spectra summed over the detector when the probe is on a column of atoms and in the hole between columns. The inset shows an expanded view of the average counts versus energy loss.

[0001] axis so that the columns of atoms may be visualized. The CBED pattern in Fig. 1(a), which has been processed to emphasize large-angle features, is that obtained when the probe is situated atop a hole, as indicated in the inset, and assuming a probe with a defocus $\Delta f = +40$ Å (an overfocus) incident on a flake of h-BN of thickness 120 Å. These values follow from an analysis of the experimental data, as will be discussed shortly. The thickness of 120 Å is reasonably consistent with an estimated thickness of 160 ± 30 Å from the EELS data, taking into account that there could well be contamination layers of amorphous carbon on the surfaces of the specimen.

Averaged spectra, when the probe is on a column (35 equivalent probe positions) or in the hole at the center of a hexagon (18 probe positions), are shown in Fig. 1(b) normalized by the integrated spectral intensity between −0.2 and 5 eV energy loss. The same spectra normalized to the maximum of the zero-loss peak are shown in Fig. 1(c). In this on-axis geometry, it is necessary to normalize the spectra to either the phonon EEL spectrum integral or to the zero-loss peak (ZLP) intensity to extract the phonon scattering contribution, as briefly discussed in Ref. [4]. The vibrational peak intensity being approximately 0.002 times that of the ZLP, along with a significant overlap with the ZLP tail, means that, without normalization, any relative atomic-scale changes in the phonon signal [Figs. 1(b) and 1(c)] are effectively "drowned out" by the elastic scattering tail—as illustrated by the un-normalized data in Fig. 1(d). The point to note is that, irrespective of which normalization procedure is used, the phonon scattering signal when the probe is in the holes is greater than when it is on the columns.

In Figs. 1(b) and 1(c), phonon-loss peaks are clearly observable between 170 and 200 meV and are attributable to combined contributions from the longitudinal (L) and transverse (T) optical (O) phonon branches as well as surface phonon polaritons (PPs) [13,14]. The PPs appear at energy losses between the TO and LO bulk modes [13–16]. The PP contribution is significant for small momentum transfers when the detector is at the BF position, as it is here. However, for the energy resolution used here (27 meV, the full width at half maximum of the ZLP), chosen to maximize the signal-to-noise ratio, and with the probe away from any sample edge, all contributions merge into a single "LO/TO/PP" loss peak when the detector is on axis. This is consistent with calculations [13,14]. As discussed in Ref. [6], the sensitivity to the probe position of the spectrum in the LO/TO/PP region at the atomic scale is strongly damped relative to an off-axis detector sampling larger values of momentum transfer.

The spectral map in Fig. 2(a) was obtained by simply dividing the raw spectral map in Fig. 2(b) (which itself was initially normalized by acquisition time) by the simultaneously acquired experimental ZLP map in Fig. 2(c). The raw spectral map for energy losses in the region from 170 to 200 meV in Fig. 2(b) yields a contrast that is rather similar to that of the ZLP map in Fig. 2(c). This is not unexpected since, for an on-axis detector, there will be both a very delocalized dipole contribution from the LO/TO/PP peak and a highly localized impact scattering contribution to the spectral map in Fig. 2(b). Due to the considerable charge transfer to the N atoms [14,17], the dipole contributions dominate [18]. Furthermore, due to the small scattering angles involved in the delocalized dipole transitions, the dipole component will have a contrast very similar to the elastic scattering, and the ratio of these two components should be close to constant. Therefore dividing the spectral map in Fig. 2(b) by the ZLP map in Fig. 2(c) yields the map in Fig. 2(a) with atomic-scale contrast that can mainly be attributed to localized impact scattering. Comparing this spectral map to that for impact phonon scattering calculated in the QEP model [10], shown in the overlay in Fig. 2(d), we see a contrast similar to that in Fig. 2(a). Both Figs. 2(a) and 2(d), which are in good agreement, show a contrast reversal relative to the map obtained from the experimental ZLP shown in Fig. 2(c). The latter is itself further validated by the simulated

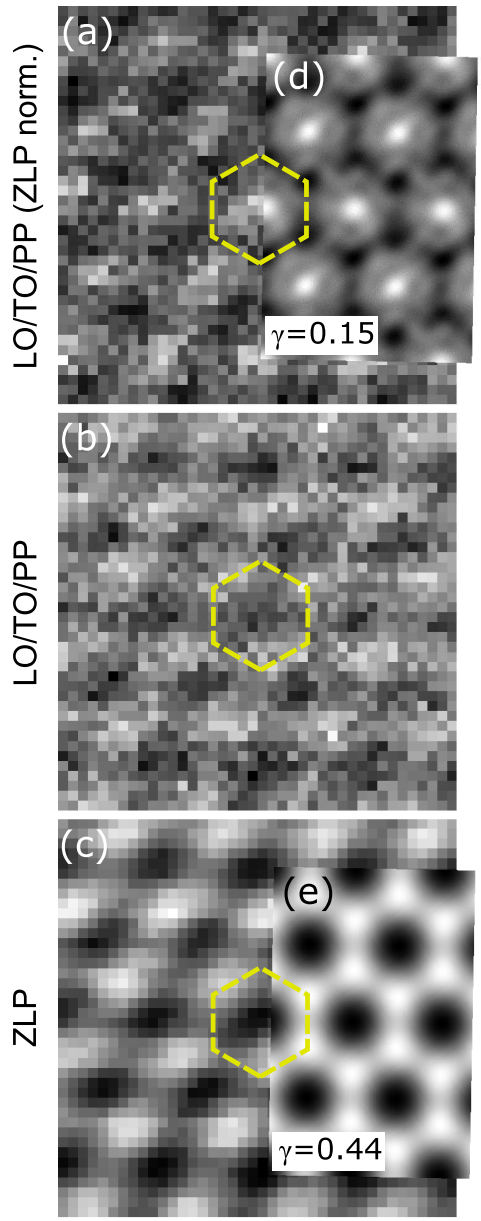

FIG. 2. (a) Experimental LO/TO/PP (170 → 200 meV) spectral image map, a function of probe position, normalized to the zero-loss peak. (b) LO/TO/PP (170 → 200 meV) raw spectral image data. (c) Experimental zero-loss (elastic) map (−10 → 10 meV). (d) Simulated spectral image for the phonon sector of the energy-loss spectrum calculated using the QEP model (only impact scattering). (e) A simulated zero-loss map. The contrast $\gamma = (\max - \min)/(\max + \min)$ is indicated in (d) and (e). The vertices of the yellow dashed hexagons indicate the location of atomic columns and set the scale (1.45 Å per side) and also serve as a guide for the eye.

map for elastic scattering into the EELS detector shown in Fig. 2(e).

The assertion in the previous paragraph that dividing the spectral map in Fig. 2(b) by the ZLP map in Fig. 2(c) yields a map in Fig. 2(a) that can mainly be attributed to localized impact scattering is further supported by an illustrative, approximate calculation in Appendix A, the results of which are illustrated in Fig. 6. We note, furthermore, that a simple ZLP tail background subtraction also results in a map (see Fig. 7 in Appendix A), with contrast similar to that of Fig. 2(b), indicating that routine background subtraction is not sufficient for extracting the phonon scattering contribution. One can speculate why this might be the case. The LO/TO/PP peak intensity is ∼0.002 times that of the ZLP, making variations in detector noise and ZLP peak shape (e.g., due to magnetic field instabilities) significant potential sources of error when attempting ZLP tail subtraction. Moreover, in Figs. 1(b) and 1(c) we clearly see a systematic broadening of the ZLP in holes: this is thought to arise from an increase in unresolved phonon signal in holes, in line with our main conclusions in this paper. It is not straightforward to take into account unresolved phonon scattering contributions in any background subtraction procedure, and doing so necessarily introduces its own errors. Extracting the phonon loss signal for an on-axis detector needs to correct for elastic scattering [4], and normalizing the LO/TO/PP peak map to the ZLP map, as described in the previous paragraph, is less prone to processing errors and yields a result which is in good agreement with theory.

The QEP model results in Fig. 2(d) were calculated using an Einstein model—a very good approximation which yields the same integrated spectrum as that obtained in a correlated model [19], where Debye-Waller factors were defined in terms of mean square thermal displacements of 0.007 Å^2 for B and 0.011 Å^2 for N. The integrity of this procedure was confirmed by Zeiger and Rusz [20], who showed explicitly that a more detailed approach that includes the correlated motion of atoms based on molecular dynamics yields results very similar to the Einstein model for such spectral maps. The simulated maps in Figs. 2(d) and 2(e) are obtained for a defocus $\Delta f = +40$ Å (overfocus) and for a sample thickness of 120 Å (18 unit cells). The simulations shown in Fig. 2 used an 8×8 supercell and 600 different atomic configurations per probe position. The defocus and thickness values were refined using simulated defocus-thickness tableaus covering a suitable range of defocus and thickness for comparison with the experimental phonon and zero-loss images shown in Figs. 2(d) and 2(e), as well as HAADF images of the same sample region (not shown). A tableau for the phonon map is shown in Appendix B.

III. CHANNELING

The zero-loss map in Fig. 2(c) does not show the contrast reversal otherwise seen for the map in Fig. 2(a) formed by electrons that have undergone localized inelastic scattering and excited a phonon, i.e., for thermal diffuse scattering (TDS). This can be understood in terms of channeling and its effect on the angular intensity distribution for TDS. In general terms, when the probe is positioned atop a column, it is strongly attracted to and localized on the column. This is illustrated in Fig. 3(a) by the probe intensity distributions at various depths through the sample for two defocus values. When the probe is in a hole, the coupling to atomic columns is not as strong, and the intensity on columns tends to be more delocalized while simultaneously having significant probability density between columns. For $\Delta f = +40$ Å the probe intensity is even distributed over several columns. In other

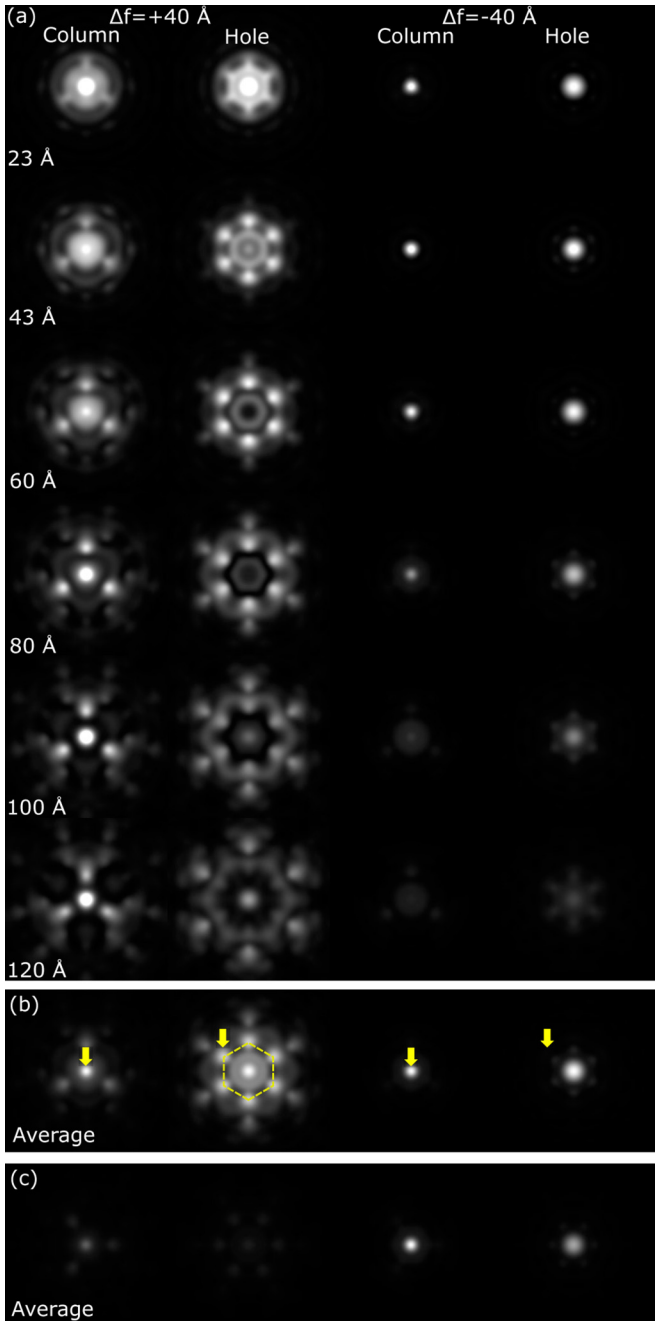

FIG. 3. (a) Probe intensities at selected depths in the specimen for the defocus values $\Delta f = +40$ Å (overfocus) and $\Delta f = -40$ Å (underfocus) and for the probe positioned on a column and in a hole in each case. Each subfigure is centered on the probe position, and each column is on a common gray scale. (b) Probe intensities averaged over the thickness of the specimen, where each subfigure is on its own gray scale. (c) Probe intensities averaged over the thickness of the specimen plotted on a common gray scale. The yellow hexagon in the second subfigure from the left in (b) sets the scale (1.45 Å per side) for parts (a), (b), and (c) and serves as a guide for the eye. In (b) the yellow arrows point to columns of atoms.

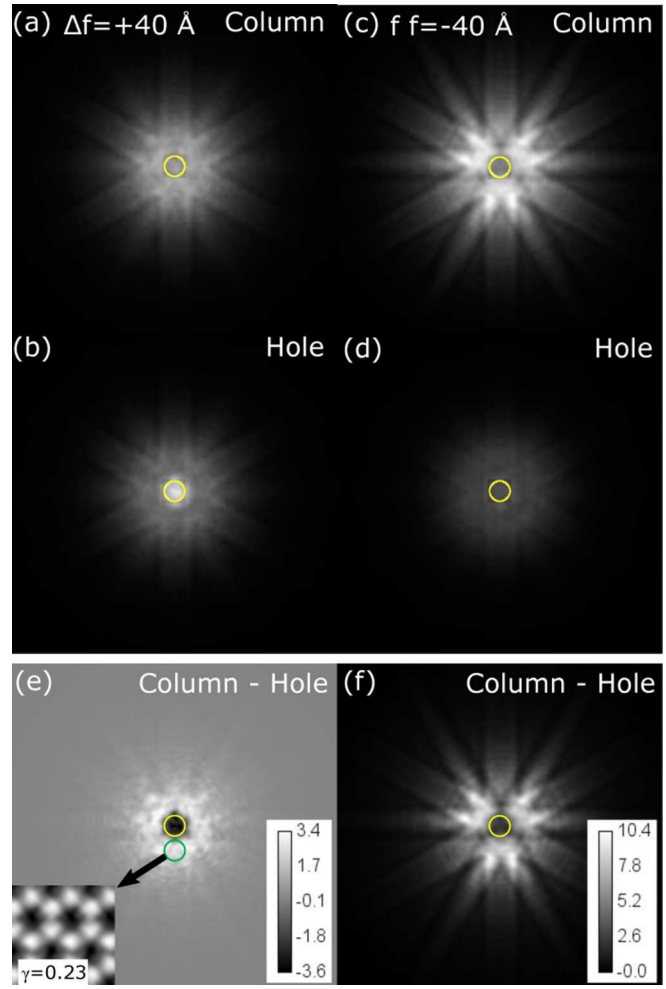

FIG. 4. (a) Distribution of electrons that have excited a phonon (or phonons) in the diffraction plane, with the probe defocused by $\Delta f = +40$ Å (overfocus) on a column with a boron atom first. The 13-mrad semi-angle entrance aperture of the EELS detector is indicated by the yellow circle. (b) As in (a), but now with the probe in the hole at the center of the h-BN lattice. (c) and (d) are the same as (a) and (b), but now for a defocus of $\Delta f = -40$ Å (underfocus). (a)–(d) are shown on a common gray scale. (e) The distribution in (a) minus that in (b) (the $\Delta f = +40$ Å case); gray is zero, and lighter colors are positive. The inset shows the spectral map obtained using a detector with an aperture positioned as indicated by the green circle. (f) The same as (e), but now subtracting the distribution in (d) from that in (c) (the $\Delta f = -40$ Å case), and now black is zero, and all other values are positive. The contrast $\gamma = (\max - \min)/(\max + \min)$ is indicated in the inset in (e). The calibration bars in (e) and (f) are fractional intensities (relative to the incident flux) in units of 10^{-6}. The yellow and green circles denote the extent of EELS detector apertures with semiangles of 13 mrad in the diffraction plane.

words, the more localized probe-sample interaction when the probe is initially placed on atomic columns leads to phonon excitation with more electrons being inelastically scattered to larger angles, in particular outside the 13-mrad aperture, as can be seen in Figs. 4(a) and 4(c). Conversely, when the probe is in the holes, there is less scattering outside of the detector aperture due to a more delocalized probe-sample interaction. Arguments along these lines were also made in Ref. [4]. Thus the TDS contrast reversal in Fig. 2(a) is intuitively a direct consequence of channeling of the probe, a point which we will now discuss more formally.

The simulation of the spectral map in Fig. 2(d) was obtained using the QEP model [10]. That model considers different atomic configurations that can be "seen" by a *single* electron and implicitly takes into account all the inelastic transitions from a ground state of the nuclear subsystem to another with the appropriate loss of energy; see Eq. (14) and related discussion in Ref. [10]. To explore the physics we shall revert to considering each inelastic transition, with an explicitly associated energy loss. We take as our starting point the following equation describing an inelastic scattering event that occurs at a specific slice z_i into the specimen, measured from the entrance surface of the specimen and along the optical axis and for one of the QEP configurations [21–24]:

$$\psi_n(\mathbf{R}, \mathbf{r}, z_i) = -i\sigma_n H_{n0}(\mathbf{r}, z_i)\psi_0(\mathbf{R}, \mathbf{r}, z_i). \quad (1)$$

The probe "wave function" ψ_0 (termed an auxiliary function in the QEP model) at the depth z_i depends on the coordinate $\mathbf{r}$ in a plane perpendicular to the optical axis, and $\mathbf{R}$ is the probe position on the surface of the specimen. The projected inelastic transition potential H_{n0} describes an inelastic transition (excitation of a phonon or phonons) via a Coulomb interaction at the depth z_i from an initial state of the specimen labeled 0 to a final state labeled n, and its modulus squared gives the probability that the transition will occur [22]. Here, $\sigma_n = m/2\pi\hbar^2 k_n$ is the interaction constant for the fast electron after energy loss, in which m is the relativistic mass of the electron and k_n is the wave number of the fast electron after the inelastic transition.

Assuming that after the inelastic event we can ignore channeling of the energy-loss electron, the wave function in the diffraction plane is given by the Fourier transform of Eq. (1):

$$\Psi_n(\mathbf{R}, \mathbf{q}, z_i) = -i\sigma_n \int H_{n0}(\mathbf{r}, z_i)\psi_0(\mathbf{R}, \mathbf{r}, z_i)e^{-2\pi i\mathbf{q}\cdot\mathbf{r}}d\mathbf{r}. \quad (2)$$

The intensity in the diffraction plane from the slice at depth z_i from all possible transitions $0 \rightarrow n$ is, multiplying by a current conversion factor k_n/k_0 [25],

$$I(\mathbf{R}, \mathbf{q}, z_i) = \sum_{n\neq 0} \frac{k_n}{k_0}|\Psi_n(\mathbf{R}, \mathbf{q}, z_i)|^2 = \sum_{n\neq 0} \frac{k_n}{k_0}\sigma_n^2 \left| \int H_{n0}(\mathbf{r}, z_i)\psi_0(\mathbf{R}, \mathbf{r}, z_i)e^{-2\pi i\mathbf{q}\cdot\mathbf{r}}d\mathbf{r} \right|^2. \quad (3)$$

The channeling of the energy-loss electron is not an essential detail since, for a large enough acceptance angle on the detector, the subtleties due to the subsequent channeling of the inelastically scattered electron are averaged over [26,27]. While the detector used here has an acceptance semiangle of 13 mrad, this is a reasonable assumption for the purposes of this discussion of the physics, and the channeling of the inelastically scattered electrons is included in the simulations.

The total signal from inelastic transitions at different depths z_i is the incoherent sum of these intensities. Equation (3) makes it absolutely clear, through the presence of the $\psi_0(\mathbf{R}, \mathbf{r}, z_i)$ term describing the probe in plane z_i inside the specimen, that the measured signal depends on how the probe wave function has scattered through the specimen to that plane.

The localization of the term $H_{n0}(\mathbf{r}, z_i)\psi_0(\mathbf{R}, \mathbf{r}, z_i)$ in Eq. (3) will determine the distribution of $I(\mathbf{R}, \mathbf{q}, z_i)$ in the diffraction plane via the Fourier transform—a localized function in real space is delocalized in the transform space and vice versa. Consider the first column in Fig. 3(a), where $|\psi_0(\mathbf{R}, \mathbf{r}, z_i)|^2$ at several depths in the specimen, averaged over the different configurations used in the QEP model, is plotted for a defocus $\Delta f = +40$ Å and with the probe on a column (with the boron atom first for this specific column). The average over thickness (using twice as many thickness values than the six shown) in Fig. 3(b) or 3(c) shows that $H_{n0}(\mathbf{r}, z_i)\psi_0(\mathbf{R}, \mathbf{r}, z_i)$ will therefore also be localized on an atomic column. This then means that, on average, the scattered intensity is biased towards relatively large momentum transfers $\mathbf{q}$, as can be seen in Fig. 4(a), where the distribution of thermally scattered electrons from all depths in the 120-Å-thick crystal is shown calculated in the QEP model (and also here including channeling for those electrons). This should be compared to the case where the probe is in a hole and not strongly localized on atomic columns, as shown in the second column of Fig. 3(a). In that case the scattering is instead biased towards small $\mathbf{q}$ values, as can be seen in Fig. 4(b). Figure 4(e) shows the result in Fig. 4(b) subtracted from that in Fig. 4(a), and in Fig. 4(e) gray corresponds to zero so that the dark (and hence negative) values inside the detector imply a contrast reversal. This occurs despite the fact that overall, there is more TDS when the probe is on a column. However, if we were to deflect the diffraction pattern by approximately 30 mrad to form the spectral map from energy-loss electrons that are inside the green circle (which has a semiangle of 13 mrad), then the contrast reversal would be avoided, as can be seen in Fig. 4(e).

It is interesting to contrast the results in Fig. 3(a) for a defocus $\Delta f = +40$ Å (overfocus) with those with $\Delta f = -40$ Å (underfocus), with the latter value chosen to provide a symmetry between the overfocus and underfocus values. In the latter case we see that the probe remains tightly bound to the column when the probe is on a column and remains largely in the hole between the columns when it is situated there. In Fig. 4(c) we see that when the probe is on the column there is a bias towards scattering to large angles, as expected. When the probe is positioned above a hole, Fig. 4(d), it is more diffuse and interacts with longer-range transition potentials on surrounding columns. There is overall less TDS, and the scattering is more biased towards small angles. It turns out that the difference between the signal into a 13-mrad detector when the probe is on a column or in a hole is small, as can be seen in Fig. 4(f), where black corresponds to zero and all other values are positive, suggesting no overall contrast reversal but lower contrast in this case. This is consistent with experimental results taken for underfocus values; an example is shown in Appendix C. Once again, we make the general observation that, for underfocus, deflecting the diffraction pattern so that an area with maximum intensity and contrast is incident on the detector would optimize the information which is experimentally available.

A strategy to avoid contrast reversals and also to optimize the signal from electrons that have excited a phonon is to use an annular detector [16]. One might think that an annulus spanning a radius where the signal appears strongest in

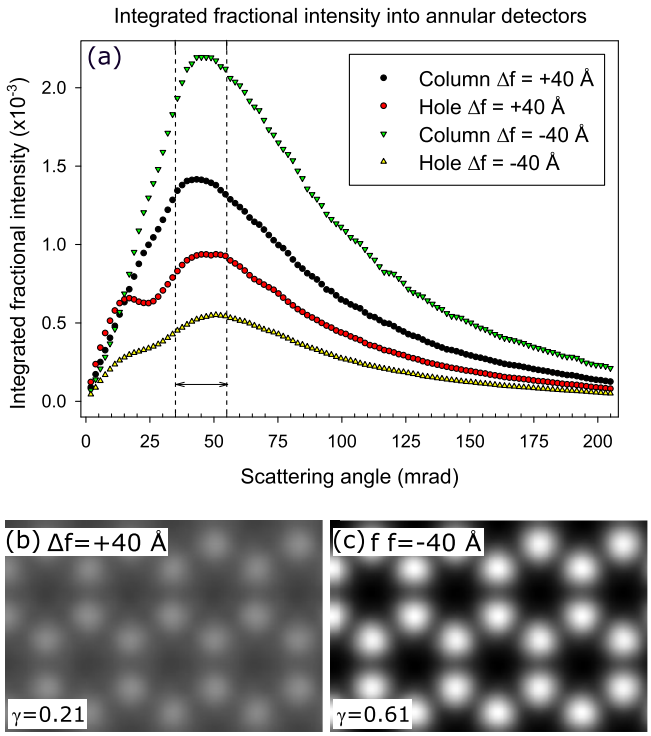

FIG. 5. (a) Integrated fractional intensity into annuli with an outer angle at the points shown and 1.88 mrad wide. The scattering angle covers the range up to the largest annulus that can be constructed in Figs. 4(a)–4(d). (b) Spectral map as a function of probe position for defocus $\Delta f = +40$ Å and for an annular detector spanning 35 to 55 mrad, as indicted in (a). (c) Same as (b), but for a defocus $\Delta f = -40$ Å. (b) and (c) are plotted on a common gray scale. The contrast $\gamma = (\max - \min)/(\max + \min)$ is indicated in (b) and (c).

Figs. 4(a)–4(d) would be the best option, but that does not take into account the increasing area of a detector covering a fixed angular range as one moves outwards in the diffraction plane. In Fig. 5(a) it can be seen that an annular aperture for the spectrometer situated around 45 mrad is likely to be optimal in this case, and this can be compared to a similar analysis for strontium titanate [28]. Figure 5(a) shows the integrated fractional intensity into annuli with outer angles at the points shown and 1.88 mrad wide. The results were obtained using the distributions of thermally scattered electrons in the diffraction plane shown in Figs. 4(a)–4(d). In Fig. 5(b) we show a spectral map as a function of probe position for defocus $\Delta f = +40$ Å. There is no contrast reversal; the maxima are on atomic columns, and contrast $\gamma = 0.21$. As we might expect from the results shown in Fig. 5(a), there is substantially more contrast for the equivalent result for $\Delta f = -40$ Å and the contrast $\gamma = 0.61$. So, in terms of contrast, defocus clearly matters. It is interesting to note that the average elastic signal into the detector for the annular range 35–55 mrad is close to a factor of 3 more than the inelastic contribution from electrons which have excited phonons (for both defocus values). Also, standard HAADF images, based on an annular aperture spanning 80–209 mrad, have a contrast very similar to each of the images shown in Figs. 5(b) and 5(c). Last, approximately 1.8 times as many electrons contribute to the HAADF image as contribute to the spectral map based on the annular detector, bearing in mind, of course, the considerably larger area of the HAADF detector. Construction of an annular detector and its use will be the subject of future work.

IV. DISCUSSION AND CONCLUSIONS

We have shown that the atomic-scale variations in the vibrational energy-loss spectrum from a thin flake of hexagonal boron nitride as an atomic-sized probe is scanned across the specimen can show apparent reversals of contrast for an on-axis detector. We have explained this phenomenon in terms of the channeling of the incident probe and suggested conditions which may mitigate the effects of contrast reversal and are more likely to provide atomic column-by-column spectroscopic information on the phonon response of a specimen and also optimize the signal.

ACKNOWLEDGMENTS

SuperSTEM is the U.K. National Research Facility for Advanced Electron Microscopy, supported by the Engineering and Physical Sciences Research Council (EPSRC).

APPENDIX A: ZLP SUBTRACTION

As asserted in the discussion of Fig. 2, dividing the phonon map in Fig. 2(b) by the ZLP (elastic map) in Fig. 2(c) should be approximately a constant if the phonon map were only due to the dipole contribution. However, this is not the case, and the residual atomic-scale inverted contrast is due to the impact phonon scattering contribution into the 13-mrad

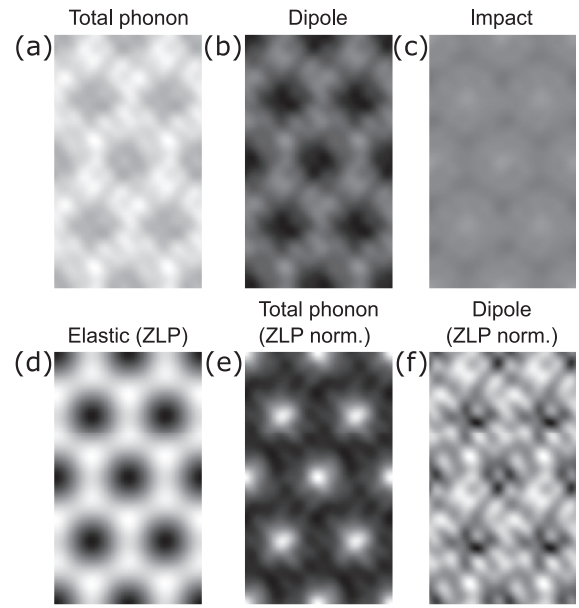

FIG. 6. (a) Total spectral map for both dipole and impact scattering. (b) Dipole component. (c) Impact component. (a) to (c) are plotted on a common gray scale. (d) Elastic (ZLP) contribution for the ionic calculation. (e) Total phonon signal in (a) divided by the ZLP map in (d). (f) Dipole contribution to the phonon spectral map in (b) divided by the ZLP map in (d).

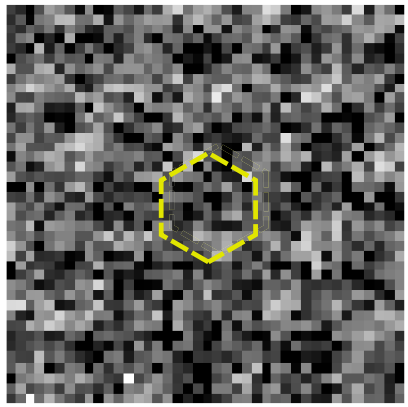

FIG. 7. Experimental ZLP subtracted LO/TO/PP (170 → 200 meV) spectral image. The vertices of the yellow dashed hexagons indicate the location of atomic columns and set the scale (1.45 Å per side) and also serve as a guide for the eye.

detector. To illustrate this point, we simplistically modeled dipole scattering in the QEP model by using (approximate) ionic scattering factors. In the paper by Yamamura *et al.* on the charge density of hexagonal boron nitride [17] it is stated that "in a simple expression of charge transfer of this material, it may be said that almost three electrons leave from the B atom. The two electrons out of these three electrons go to N atoms to form N^{2-} anions and the rest of the electrons remain in [the] interatomic region." Let us approximate this even further and assume a transfer of two electrons from B to N. We then construct approximate ionic atomic scattering factors for B and N using the closest neutral atom containing the same number

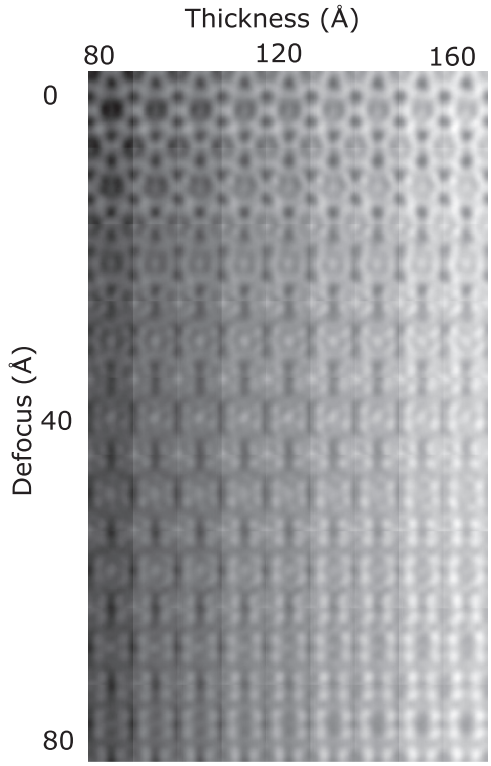

FIG. 8. Defocus-thickness tableau for which the simulation in Fig. 2(d) corresponds to the central unit cell.

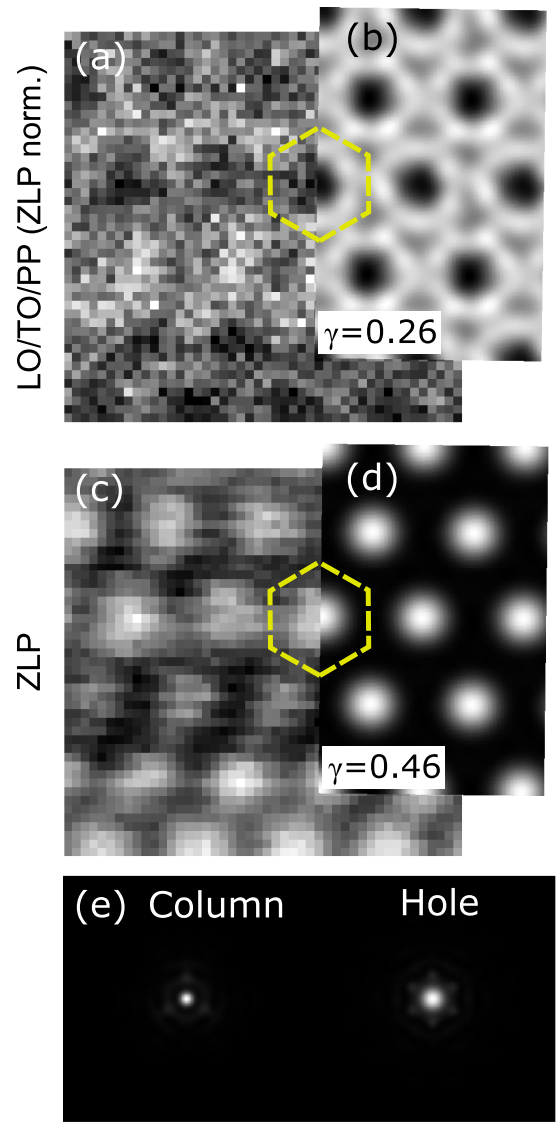

FIG. 9. Spectral images for a probe defocus $\Delta f = -90$ Å (underfocus). (a) Experimental LO/TO/PP (170 → 200 meV) spectral image normalized to the zero-loss peak. (b) Simulated spectral image for the phonon sector of the energy-loss spectrum calculated using the QEP model. (c) Experimental zero-loss (elastic) map (−10 → 10 meV) as a function of probe position. (d) A simulated zero-loss map. (e) Probe intensities averaged over the thickness of the specimen. The contrast $\gamma = (\max - \min)/(\max + \min)$ is indicated in (b) and (d). The vertices of the yellow dashed hexagons indicate the location of atomic columns and set the scale (1.45 Å per side) and also serve as a guide for the eye.

of electrons as the ion from the parametrization of Waasmaier and Kirfel [29] to approximate the electronic structure, but we explicitly include the correct ionic contribution for smaller scattering angles. This calculation gives the approximation for the total phonon spectral map (dipole plus impact contributions) shown in Fig. 6(a). The dipole contribution in Fig. 6(b) was estimated by subtracting from Fig. 6(a) the impact component from a calculation with no charge transfer, shown in Fig. 6(c). Figures 6(a) to 6(c) are plotted on a common gray scale, and Fig. 6(c) is the same result shown in Fig. 2(d) in the

main text, but with the contrast damped due to the common gray scale. The elastic (ZLP) contribution using the ionic scattering factors is shown in Fig. 6(d). Figure 6(e) shows the total phonon signal in Fig. 6(a) divided by the ZLP map in Fig. 6(d)—this is analogous to how the experimental data have been treated. Figure 6(f) is therefore the approximately obtained dipole contribution to the phonon spectral map in Fig. 6(b) divided by the ZLP map in Fig. 6(d). The contrast shown in Fig. 6(f) is not inverted and is, roughly speaking, more uniform than that in Fig. 6(b); it is the impact scattering component, scattering which is contained within the total phonon signal, that manifests itself in a contrast reversal. This supports, albeit in an approximate and somewhat simplistic way, the normalization procedure that has been used.

Figure 7 shows a spectral map for energy losses of 170 to 200 meV formed after ZLP subtraction. The elastic tail contribution was estimated by fitting of a power-law function over the energy-loss region from 97 to 130 meV. The contrast of the ZLP subtracted map, being quite similar to that of the corresponding raw spectral map in Fig. 2(b), is, as discussed above, dominated by elastic scattering. Clearly, in this on-axis geometry routine ZLP tail subtraction is insufficient for extracting the phonon scattering contribution from the vibrational STEM-EELS data acquired.

APPENDIX B: DEFOCUS-THICKNESS TABLEAU

Figure 8 shows a thickness-defocus tableau for which the simulation in Fig. 2(d) corresponds to the central unit cell. The defocus and thickness are varied in steps of 10 Å, and a single unit cell is displayed for each pair of defocus and thickness values. The simulations used a 4×4 supercell, and 600 atomic configurations were used for each probe position.

APPENDIX C: UNDERFOCUS

Figure 9(a) shows an experimental LO/TO/PP spectral map, normalized to the ZLP and acquired at an underfocus of $\Delta f = -90$ Å. The energy resolution was 28 meV, as given by the full width at half maximum of the ZLP. The defocus and thickness (120 Å) values were refined by comparing simulated defocus-thickness tableaus (covering a suitable range of defocus and thickness) with the experimental phonon and zero-loss images in Figs. 9(a) and 9(c), as well as HAADF images of the same sample region (not shown). Simulations for this defocus and thickness value in the QEP model are the overlays shown as Figs. 9(b) and 9(d). The defocus value identified here, $\Delta f = -90$ Å, is a greater defocus than $\Delta f = -40$ Å used for comparison purposes with $\Delta f = +40$ Å in Sec. III. However, the channeling behavior of the probe is, in general, similar to that of the $\Delta f = -40$ Å probe, as can be seen by comparing the averaged probe intensities in Fig. 9(e) with the rightmost two intensities in Fig. 3(b).

In Fig. 9(a) the contrast is clearly higher on the atomic columns than in the holes, in good agreement with the simulated spectral image for the phonon sector of the energy-loss spectrum in Fig. 9(b). As discussed in Sec. III, this reversal of contrast compared to the experimental LO/TO/PP map acquired at overfocus [$\Delta f = +40$ Å, Fig. 2(a)] is a consequence of channeling of the electron probe. The slight minima on atomic sites in Fig. 9(b) are attributable to more scattering to larger angles when the probe is on a column and couples to it more strongly than when it is just off a column. However, when comparing intensities with the probe on or in the vicinity of a column and when it is a hole, there is no overall contrast reversal in the sense that the intensity is at a maximum in the holes.

[1] O. L. Krivanek, T. C. Lovejoy, N. Dellby, T. Aoki, R. W. Carpenter, P. Rez, E. Soignard, J. Zhu, P. E. Batson, M. J. Lagos, R. F. Egerton, and P. A. Crozier, Nature (London) **514**, 209 (2014).

[2] T. Miyata, M. Fukuyama, A. Hibara, E. Okunishi, M. Mukai, and T. Mizoguchi, Microscopy **63**, 377 (2014).

[3] T. C. Lovejoy, G. C. Corbin, N. Dellby, M. V. Hoffman, and O. L. Krivanek, Microsc. Microanal. **24**, 446 (2018).

[4] K. Venkatraman, B. D. Levin, K. March, P. Rez, and P. A. Crozier, Nat. Phys. **15**, 1237 (2019).

[5] O. L. Krivanek *et al.*, Ultramicroscopy **203**, 60 (2019).

[6] F. S. Hage, D. M. Kepaptsoglou, Q. M. Ramasse, and L. J. Allen, Phys. Rev. Lett. **122**, 016103 (2019).

[7] H. Gawronski, M. Mehlhorn, and K. Morgenstern, Science **319**, 930 (2008).

[8] K. Volgmann, H. Gawronski, Ch. Zaum, G. G. Rusina, S. D. Borisova, E. V. Chulkov, and K. Morgenstern, Nat. Commun. **5**, 5089 (2014).

[9] F. Hage, G. Radtke, D. Kepaptsoglou, M. Lazzeri, and Q. Ramasse, Science **367**, 1124 (2020).

[10] B. D. Forbes, A. V. Martin, S. D. Findlay, A. J. D'Alfonso, and L. J. Allen, Phys. Rev. B **82**, 104103 (2010).

[11] A. Shmeliov, J. S. Kim, K. B. Borisenko, P. Wang, E. Okunishi, M. Shannon, A. I. Kirkland, P. D. Nellist, and V. Nicolosi, Nanoscale **5**, 2290 (2013).

[12] G. Constantinescu, A. Kuc, and T. Heine, Phys. Rev. Lett. **111**, 036104 (2013).

[13] F. S. Hage, R. J. Nicholls, J. R. Yates, D. G. McCulloch, T. C. Lovejoy, N. Dellby, O. L. Krivanek, K. Refson, and Q. M. Ramasse, Sci. Adv. **4**, eaar7495 (2018).

[14] R. J. Nicholls, F. S. Hage, D. G. McCulloch, Q. M. Ramasse, K. Refson, and J. R. Yates, Phys. Rev. B **99**, 094105 (2019).

[15] A. A. Govyadinov *et al.*, Nat. Commun. **8**, 1 (2017).

[16] C. Dwyer, T. Aoki, P. Rez, S. L. Y. Chang, T. C. Lovejoy, and O. L. Krivanek, Phys. Rev. Lett. **117**, 256101 (2016).

[17] S. Yamamura, M. Takata, and M. Sakata, J. Phys. Chem. Solids **58**, 177 (1997).

[18] C. Dwyer, Phys. Rev. B **96**, 224102 (2017).

[19] B. D. Forbes and L. J. Allen, Phys. Rev. B **94**, 014110 (2016).

[20] P. M. Zeiger and J. Rusz, Phys. Rev. Lett. **124**, 025501 (2020).

[21] W. Coene and D. Van Dyck, Ultramicroscopy **33**, 261 (1990).

[22] C. Dwyer, Ultramicroscopy **104**, 141 (2005).

[23] S. D. Findlay, M. P. Oxley, and L. J. Allen, Microsc. Microanal. **14**, 48 (2008).
[24] L. J. Allen *et al.*, Ultramicroscopy **151**, 11 (2015).
[25] S. L. Dudarev, L.-M. Peng, and M. J. Whelan, Phys. Rev. B **48**, 13408 (1993).
[26] T. W. Josefsson and L. J. Allen, Phys. Rev. B **53**, 2277 (1996).
[27] C. Dwyer, S. D. Findlay, and L. J. Allen, Phys. Rev. B **77**, 184107 (2008).
[28] N. R. Lugg, B. D. Forbes, S. D. Findlay, and L. J. Allen, Phys. Rev. B **91**, 144108 (2015).
[29] D. Waasmaier and A. Kirfel, Acta Crystallogr., Sect. A **51**, 416 (1995).